Ultra-Compact Non-Travelling-Wave Silicon Carrier-Depletion Mach-Zehnder Modulators Towards High Channel Density Integration

Guangwei Cong, *Member, IEEE*, Yuriko Maegami, Morifumi Ohno, and Koji Yamada, *Senior Member, IEEE*

***Abstract*—Silicon Mach-Zehnder modulators (MZMs) utilizing carrier depletion usually adopt traveling-wave (TW) electrodes for their long phase shifters, which have inherent challenges in miniaturization, limiting the integration density of monolithic transceivers. In this work, we experimentally demonstrate non-TW carrier-depletion MZMs that give better compromises between compact footprint, modulation depth, and high speed. They adopt densely meandered phase shifters and thus offer an ultra-compact lumped-element MZM for using carrier depletion. Up to 28.1 Gb/s NRZ eye diagrams and ∼26 GHz electro-optic bandwidth were experimentally achieved. The proposed lumped circuit model well explains the experimental data, indicating that impedance mismatching is the dominant factor in determining experimental bandwidth and a LC resonance contributes to the bandwidth improvement. Driving configurations with better impedance matching are proposed to further improve bandwidth. This novel MZM can enhance the integration density of modulators in wavelength-division multiplexing transceivers.**

***Index Terms*—Electrooptic modulators, Silicon photonics.**

I. Introduction

OPTICAL transceivers are continuously miniaturized for low-cost, low-power, and high-density optical interconnects [1]. Silicon photonics are believed as a leading technology to realize such transceivers due to its integration compatibility and will be more competitive than ever when co-packaging or monolithically integrating with electrical circuits becomes available [2]–[4]. On the one hand, integrating silicon photonics with electronics is becoming a disruptive hardware solution to build ultra-dense high-complexity electro-optic circuits. On the other hand, multiple wavelength lanes of 400G and beyond are required for future inter/intra-data center interconnects to satisfy continuous increases in transmission capacity. If adopting dense wavelength-division multiplexing, several tens or even more wavelength channels will be required. Therefore, it is very important to keep silicon photonic transceivers as compact as possible from the views of integration density, easy packaging, low power, and low cost.

Most components in silicon photonic transceivers can be made with small footprints, while Mach-Zehnder modulators (MZMs) based on carrier depletion are of large sizes. They are usually several millimeters (mm) long [5], occupying large chip areas and limiting miniaturization of transceivers. There are compact silicon modulators such as ring modulators [6], slow-light modulators [7], [8], and MZMs using carrier injection [9], [10]; whereas MZMs using carrier depletion have advantages in the wide spectral bandwidth, high speed, and low dispersion so that they remain as a competitive choice in commercialized silicon photonic transceivers [1], [11]. But due to the low modulation efficiency, they usually need long phase shifters, for which traveling-wave (TW) electrodes in form of coplanar waveguides are one of the most common electrode choices (traveling-wave driving) [5]. Another choice is to adopt distributed electrodes (multiple lumped element driving) [12]. Both choices have similar large footprints. For the former, it is difficult to obtain impedance and radio frequency (RF)-optical velocity matching simultaneously over a broad band [13], [14]. If adopting slow-wave electrode structures [15], [16], better velocity matching can be achieved. However, the RF loss is unavoidable along several-mm-long TW electrodes loaded with *pn* junction capacitance and quickly increases with the phase shifter length and frequency, which is believed as an inherent limiting factor of bandwidth [13], [14], [17]. This also means that further increasing the electrode length is not so effective to improve the high frequency modulation efficiency and velocity mismatching will become more severe as well. For the latter, the phase shifter is divided into multiple small segments and each segment can be driven at very fast speed by an individual RF signal, thus it is free of the RF-loss problem. The driver is of high complexity because there are many RF signal channels and RF-delay adjustment between channels is required to compensate optical delay in each segment. Silicon TW-MZMs based on carrier depletion have encountered bottlenecks in breaking through bandwidth and efficiency limitations. Recently advanced modulation formats with high baud rates (>70G) have been demonstrated using low-bandwidth TW-MZMs (<40 GHz in [18], [19], ∼47 GHz in [20]). It becomes more and more difficult for silicon modulators to compete on baud rates with other modulators such as lithium niobate [21], [22] and InP modulators [23] due to intrinsic material limitation. Tremendous efforts have been spent

Manuscript received July 29, 2020; revised September 8, 2020; accepted September 24, 2020. Date of publication September 29, 2020; date of current version October 22, 2020. *(Corresponding author: Guangwei Cong.)*

The authors are with the Research Institute for Advanced Electronics and Photonics, National Institute of Advanced Industrial Science and Technology, Tsukuba 305-8569, Japan (e-mail: gw-cong@aist.go.jp; yuriko-maegami@aist.go.jp; morifumi-ohno@aist.go.jp; yamada.koji@aist.go.jp).

Color versions of one or more of the figures in this article are available online at https://ieeexplore.ieee.org.

Digital Object Identifier 10.1109/JSTQE.2020.3027324

on hybrid integrated modulators on silicon using non-CMOS (complementary metal oxide semiconductor) process to seek breakthroughs, while all-silicon modulators remain competitive in large-scale integration, low cost, and high-volume production by leveraging the fully CMOS-compatible process, which are believed as the core advantages of silicon photonic transceivers. Therefore, silicon photonic transceivers will more and more rely on enhancing integration density (i.e., channel parallelization of wavelength or mode) of modulators to increase overall link capacity to compete with those on other platforms. The carrier-depletion MZMs have been extensively studied in the past as an important all-silicon modulator, while its miniaturization remains challenging compared to ring modulators and those using carrier injection and slow light.

Decreasing the phase shifter length of TW-MZMs is better for lowering the RF loss; but the modulation amplitude will also be decreased. Thus, the problem is how to compromise a small MZM footprint to make the RF loss negligible and a reasonable phase shifter length to guarantee necessary modulation amplitude. For this purpose, the lumped-element MZM could be a potential choice, for which we could adopt a single lumped-element driving instead of travelling-wave and distributed-electrode driving to keep the driver simple. In [14], using meandered phase shifter to realize lumped-element MZMs was first proposed and simulated for silicon epitaxially-grown diodes loaded with a comb-like electrode. In [24], using the same concept as that in [14], we experimentally demonstrated a non-traveling-wave (NTW) MZM (NTW- MZM) by employing a densely meandered phase shifter, which for the first time reported the experimental results of a lumped-element MZM modulator based on carrier depletion without utilizing slow-light effects [7], [8], as far as we know. Recently, in [25], a lumped-element MZM using an electrode structure different from that modeled in [14] was experimentally presented with about 8−12 GHz bandwidths within 2−5 V biases. These NTW-MZMs have quite compact footprint. As for our case, it has an ultra-compact footprint (<500 μm in width and <250 μm in length), which is almost equivalent to the electrical pad size of TW-MZMs, only 1/8∼1/16 of a usual TW-MZM, and also smaller than those of distributed [26] and multi-segmented electrode types [12]. Due to the small area, RF driving signals have no attenuation along the phase shifter, which can relatively improve the modulation efficiency for shorter phase shifters. However, compared to TW-MZMs, the high frequency bandwidth is still low. For optimizing such lumped-element MZMs, we examine the transit time effects on eye diagrams and high frequency responses under various diode conditions and perform bandwidth comparison with TW-MZMs. We also study the impedance matching with considering the effect of LC resonance on bandwidth since in our experiment we found the inductance of comb-like electrodes can contribute to bandwidth enhancement via inducing a LC resonance. These two aspects have not been fully studied yet, especially for the conventional CMOS-compatible horizontal and vertical *pn* diodes.

In this paper, we present the updated results of NTW-MZMs with bandwidth much improved compared to previous works [14], [25] and our initial work [24]. A comprehensive study on NTW-MZMs is done from aspects of design, simulation, and experiment. The paper is organized as follows. Section II presents fundamental issues of NTW-MZM, including modulator design, transit time determined bandwidth, and what *pn* junctions can fit better into NTW-MZMs than TW-MZMs. The effects of transit time on eye diagrams and frequency responses under various diode conditions are discussed and comparison with TW-MZMs are presented. Section III presents the fabricated devices, experimental results, circuit models, and discusses the impedance matching and contributions of LC resonance in enhancing bandwidths. Finally, Section IV concludes the paper.

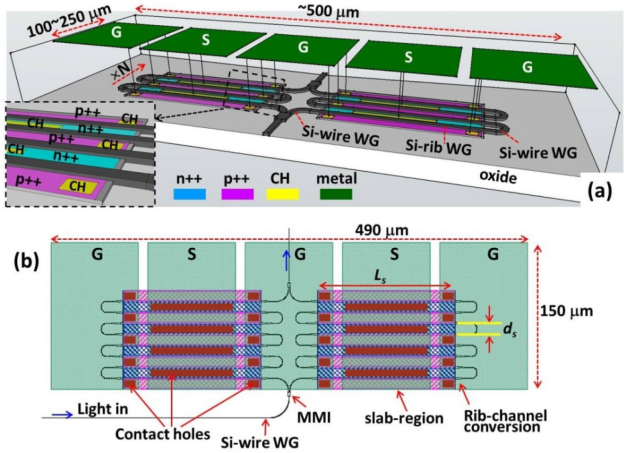

Fig. 1. (a) Schematic picture and (b) layout of the NTW-MZM. WG: waveguide. CH: contact hole. MMI: multimode interference coupler. Si: silicon.

II. Design and Simulation

A. Modulator Design

Figs. 1(a) and 1(b) show the schematic structure and layout of the proposed silicon NTW-MZM, respectively. This device can be fabricated on photonic silicon-on-insulator (SOI) wafers with a SOI thickness of 200∼300 nm. It is a MZ interferometer structure composed of two multimode interference couplers and two arms. The feature lies in that the arms are consisted of multiple parallel segments of straight rib waveguides (in slab region) which are connected at both ends by the fully etched Si-wire waveguides through the low-loss rib-channel conversion structures. The *pn* junctions are embedded in these rib waveguides as the phase shifters. Both horizontal and vertical *pn* junctions [27] are applicable. Two adjacent segments of rib waveguides are close to each other to share a middle doping region. The segment length L_s and distance d_s of rib waveguide segments are 140.5 μm and 11.3 μm, respectively. So, the total length of phase shifter is 1.124 mm for each arm using eight segments. For such a phase shifter, we have designed two kinds of MZMs with different electrode designs. Our initial design shown in Fig. 1 was presented in [24] where the contact holes to the doping regions are alternatively put at the center and two ends of rib waveguides for accessing the signal (S) and ground (G) electrodes, respectively. This design is 490 μm in width and 150 μm in length, nearly equivalent to the electrode

pad size of TW-MZMs. Our improved design uses comb-like electrode, which was also fabricated and will be discussed in Section III. With such a phase shifter design, we can realize a lumped-element carrier-depletion MZM with both a small footprint and a reasonable length of phase shifter. Note that the *S* electrodes are connecting to the *n*-side of diodes.

B. Transit Time Determined Bandwidth

The bandwidth of TW-MZMs cannot reach the resistance-capacitance (RC) bandwidth of diodes due to the factors such as RF loss, RF-optical velocity mismatching, and impedance mismatching. For the lumped-element NTW-MZM, the bandwidth is determined by optical transit time corresponding to the phase shifter length and impedance mismatching. In this section, perfect impedance matching condition is assumed, and we only consider the phase modulation induced by carrier depletion upon various diode parameters. Thus, the bandwidth discussed in this section can be regarded as the theoretical limit of NTW-MZM. The influence of impedance matching will be discussed in the experimental part in Section III.

The transit time determined bandwidth comes from the mismatch between the RF frequency and the transit time for light passing through the phase shifter, which is different from the RF-optical velocity mismatching in TW-MZMs because it is not related to the RF effective index. Here we investigate the bandwidth with considering both RC parameters and transit time. For this purpose, we iteratively solve the well-known Kirchhoff's current equation (Eq. (1)) and an integral equation (Eq. (2)) of phase shift $\Delta\phi$ in time domain. V_s and V_c are the RF source voltage and the actual voltage on junction capacitor that causes the optical phase change, respectively. R_{pn} and C_{pn} denote the series resistance and capacitance of the *pn* diodes, respectively. c_0, n_g, and η are the light speed in vacuum, group index of silicon rib waveguide, and modulation efficiency in unit of radian/(V·μm), respectively. τ_0 is the transit time for light passing through the phase shifter at its group velocity. V_s can be sinusoidal wave $V_{pp}sin(2\pi ft)/2$ for frequency response simulation or pseudo-random bit sequence (PRBS) for eye diagram simulation (V_{pp} is the peak-to-peak driving voltage). Given a phase shifter length that has a corresponding τ_0, we can calculate the frequency response $r(f) = 20log|\Delta A[\Delta\phi_m(f)]/\Delta A[\Delta\phi_m(0)]|$ for each frequency f, where ΔA is the optical modulation amplitude of MZM upon a phase modulation $\Delta\phi_m$.

$$C_{pn}\frac{dV_c}{dt} = \frac{V_s - V_c}{R_{pn}} \tag{1}$$

$$\Delta\phi(t) = \int_{t-\tau_0}^{t} \frac{\eta c_0 V_c(t)}{n_g} dt \tag{2}$$

Before simulation, we determine R_{pn}, C_{pn}, and η for three diode conditions to be studied: a horizontal *pn* junction (hPN) with a doping density of 1×10^{18} cm^{-3} and two vertical *pn* junctions (vPN) with doping densities of 1×10^{18} and 2×10^{18} cm^{-3}. Fig. 2(a) shows the schematics of the hPN and vPN, both of which are usually used in TW-MZMs [2], [27]. They are assumed to be fabricated on 220-nm SOI wafers and have the same waveguide parameters (rib width = 600 nm, slab thickness = 110 nm). The junction positions are at the horizontal and vertical centers of SOI layers for the hPN and vPN, respectively. Uniform doping is assumed for simplicity and *n* and *p* concentrations are equal. Using Lumerical simulators [28], we calculated C_{pn} and phase change $\Delta\phi$ in relation of the reverse bias (V_b), as shown in Figs. 2(b) and 2(c). To get the continuous equations of $C(V_b)$ and $\Delta\phi(V_b)$, the simulated C_{pn} and $\Delta\phi$ were fitted by the Eqs. (3) and (4), respectively, in which we used a building-in potential of 0.75 V. The fitting results are shown by the black lines in Figs. 2(b) and 2(c) and the corresponding fitting parameters are summarized in Table I. For frequency response, we perform small signal analysis so that C_{pn} and η are assumed to be constant at the operating bias of V_b = 3 V. The efficiency η (rad/V·μm) is the first order derivative of $\Delta\phi$ at $V_b = 3$ V. For eye diagram, we perform large signal analysis by including the bias dependences of C and $\Delta\phi$ according to the Eqs. (3) and (4). We use $R_{pn} = 6000$ and 4100 $\Omega\cdot\mu$m for 1×10^{18} and 2×10^{18} cm^{-3}, respectively, including both *p* and *n* doping regions. In this section, we only consider the junction capacitances of *pn* diodes, neglecting other capacitances, and all simulations were done at the quadrature point of MZM using TE polarization, 1.55-μm wavelength, and $n_g = 3.8$.

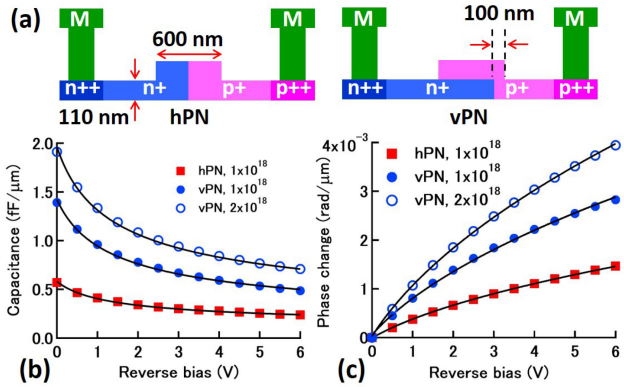

Fig. 2. (a) Horizontal *pn* (hPN) and vertical *pn* (vPN) junctions used in simulation. Bias dependences of (b) capacitance and (c) phase change. The black lines are fitting lines using Eqs. (3) and (4), respectively. M: metal.

TABLE I
FITTING PARAMETERS FOR THE BIAS DEPENDENT PHASE CHANGE ($\Delta\phi$) AND CAPACITANCE (C)

	N	$\Delta\phi(V_b)$		
	cm^{-3}	a	b	c
hPN	1×10^{18}	0.014	270.20	-7.45×10^{-4}
vPN	1×10^{18}	0.020	149.13	-1.35×10^{-3}
vPN	2×10^{18}	0.023	100.15	-1.95×10^{-3}
	N	$C(V_b)$		
	cm^{-3}	a′	b′	c′
hPN	1×10^{18}	120.67	1.36×10^{-5}	0.069
vPN	1×10^{18}	253.39	2.24×10^{-5}	0.038
vPN	2×10^{18}	272.88	3.55×10^{-5}	0.083

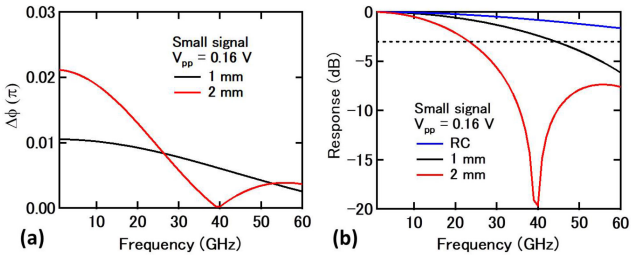

Fig. 3. (a) Frequency dependent phase shift $\Delta\phi$ and (b) corresponding frequency response of the NTW-MZM using the hPN with a doping density of 1×10^{18} cm^{-3}. The dotted line indicates -3 dB.

$$C\left(V_b\right) = a'\sqrt{\frac{b'}{0.75 - V_b}} + c' \tag{3}$$

$$\Delta\phi\left(V_b\right) = a\sqrt{\frac{0.75 - V_b}{b}} + c \tag{4}$$

First, we discuss the frequency response of NTW-MZM using the hPN with a doping density of 1×10^{18} cm^{-3}. The frequency response was simulated using $V_{pp} = 0.16$ V. The simulated phase shift $\Delta\phi$ versus frequency and the corresponding frequency response are shown in Figs. 3(a) and 3(b), respectively. The phase shifter lengths of 1 and 2 mm were simulated to clarify the influence of transit time on bandwidth. The 2-mm phase shifter has two times higher phase modulation at the low frequency side ($f \rightarrow 0$) but shows a much lower 3-dB bandwidth than the 1-mm one. The 3-dB bandwidths are about 44.3 and 23.3 GHz for 1 and 2 mm, respectively. This bandwidth difference comes from the difference in the transit time. With increasing the frequency, when the half period time ($1/2f$) becomes shorter than the transit time τ_0 ($n_g L/c_0$), the accumulated phase shift in the positive half period of RF voltage will be cancelled in the negative half period in coming. Full cancellation will occur when $f = 1/\tau_0$ ($= c_0/n_g L$) at which the time for the light passing through the phase shifter exactly equals the full RF period. Thus, $\Delta\phi = 0$ occurs $\sim$40 GHz for $L = 2$ mm ($c_0/n_g L = 39.5$ GHz). As seen in Eqs. (1) and (2), the calculated bandwidths have already included the contribution from RC constant. Because the RC bandwidth (>80 GHz) is very high, as seen in Fig. 3(b), these bandwidths are mainly dominated by the transit time.

Next, we examine the eye diagrams in response to above frequency responses under driving by a large signal ($V_{pp} = 3$ V). $2^7 - 1$ PRBS pattern was used in simulation and the waveform was generated by introducing pulse edge response $exp[-(t/\tau)^3]$ ($\tau = 18$ ps) [29]. This response corresponds to a $\sim$12 ps rising/falling time (20%–80%) which agrees well with most pulse pattern generators. Figs. 4(a) and 4(b) show the simulated eye diagrams for 1 and 2 mm, respectively. Both lengths show clear eye opening at 25 Gb/s and the extinction ratios (ER) are 2.9 and 6.7 for 1 and 2 mm, respectively. The eye can keep open for up to 56 Gb/s for 1 mm even though the ER degrades with increasing the bit rate; but for 2 mm, the eye can be opened for up to 40 Gb/s. The large-signal eye diagram results are consistent with above small-signal bandwidth analysis. Thus, the tradeoff between ER and bandwidth can be simply done by changing the total phase shifter length through changing the segment number in Fig. 1(a). Decreasing the phase shifter length can enhance the bandwidth, but the ER also decreases. Therefore, we have two questions for further improvement: (1) how to enhance the ER with a similar bandwidth; and (2) how to enhance the bandwidth with an equivalent ER. For these goals, we plan to apply the vPN shown in Fig. 2(a) to the NTW-MZM, which will be discussed in the next.

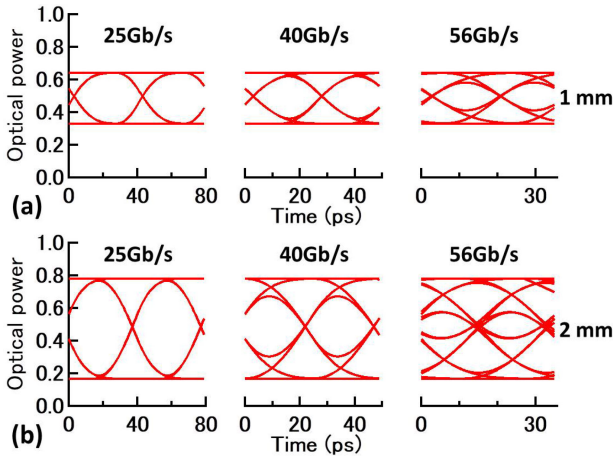

Fig. 4. Simulated eye diagrams at 25, 40, and 56 Gb/s for the NTW-MZMs with (a) 1 mm and (b) 2 mm phase shifters using the hPN with a doping density of 1×10^{18} cm^{-3}.

C. Vertical PN for NTW-MZM

Here we discuss what kinds of *pn* junctions can offer better tradeoff of figure of merits for NTW-MZMs. For traditional TW-MZMs, various diode structures were proposed to improve the modulation efficiency [30], [31]. The modulation efficiency can be enhanced by increasing the overlap integral between the depleted charge profile and the optical mode profile. Provided that the optical mode is constant, the increase in overlap means an increase in the junction area or charge density, either of which will induce the increase in junction capacitance. Thus, the decrease in bandwidth is usually observed when we try to utilize these diodes with large electro-optic (EO) overlaps to improve the modulation efficiency. However, such diodes can fit better for the NTW-MZM than the TW-MZM because the bandwidth of NTW-MZM is determined by the transit time (i.e., phase shifter length) provided that the RC bandwidth is large enough compared to that determined by the transit time. In other words, using these high-efficiency diodes, we can achieve an enhanced ER with the same phase shifter length and maintain a similar bandwidth because the transit time is not influenced by the doping profile and the junction capacitance. On the other side, we can use even shorter phase shifters to enhance the bandwidth and meanwhile maintain an equivalent ER. The vPN diode is one of such high-efficiency diodes [27], [31] and here we apply the vPN diode shown in Fig. 2(a) to the NTW-MZM.

The simulated EO responses and eye diagrams are shown in Figs. 5 and 6, respectively, for various diode conditions. The obtained 3-dB bandwidths (BW) and ER (at 25 Gb/s)

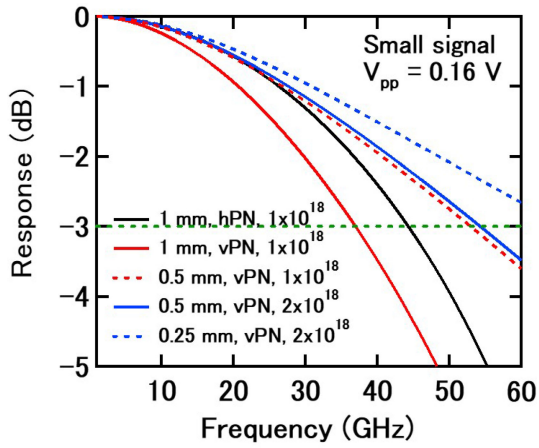

Fig. 5. Simulated EO responses of NTW-MZMs under various diode conditions. The green line indicates −3 dB.

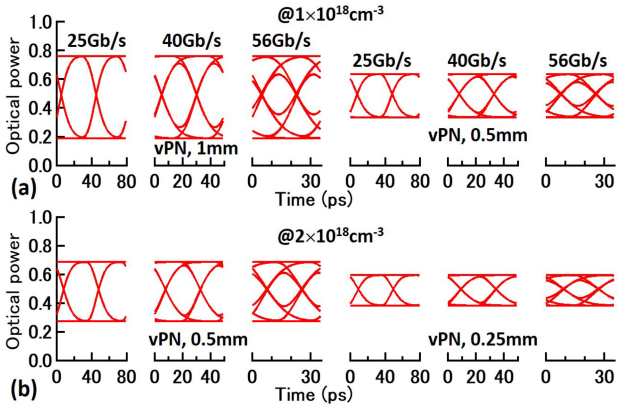

Fig. 6. Simulated eye diagrams of NTW-MZMs using vertical *pn* (vPN) junctions with the doping densities (a) 1×10^{18} and (b) 2×10^{18} cm^{-3}.

TABLE II
SUMMARY OF THE 3-DB BANDWIDTH AND EXTINCTION RATIO (ER) OF SIMULATED EYE DIAGRAMS AT 25 GB/S

	N/cm^{-3}	L/mm	BW/GHz	ER/dB
hPN	1×10^{18}	1	44.3	2.9
hPN	1×10^{18}	2	23.3	6.7
vPN	1×10^{18}	1	37.0	6.1
vPN	1×10^{18}	0.5	53.0	2.8
vPN	2×10^{18}	0.5	54.3	4.0
vPN	2×10^{18}	0.25	66.0	1.9

are summarized in Table II. For the same phase shifter length ($L = 1$ mm) and same doping density ($N = 1 \times 10^{18}$ cm^{-3}), the bandwidth of vPN (37 GHz) is ∼6 GHz smaller than that of the hPN due to the increase in the RC constant, but the vPN shows ∼2 times increase (2.9 dB → 6.1 dB) in the ER compared to the hPN. Its eye diagram remains open for the bit rates up to 56 Gb/s, as shown in Fig. 6(a). If using a 0.5-mm phase shifter, the vPN shows a bandwidth of ∼53 GHz, about 9 GHz higher than that of 1-mm hPN (44.3 GHz), and meanwhile the eye diagram shows an almost equivalent ER to that of 1-mm hPN with an improved opening. Doping density is another parameter that can be used to tune the bandwidth and ER for the NTW-MZM. For the 0.5-mm vPN, if we increase the doping density to 2×10^{18} cm^{-3}, the ER can be further improved by ∼43% and the bandwidth remains >50 GHz. This is different from the conventional tradeoff between bandwidth and ER performed for TW-MZMs because we can improve ER without sacrificing bandwidth. Note that it is due to the decrease in series resistance of diode that the increase in doping density from 1 to 2×10^{18} cm^{-3} does not result in a decrease in bandwidth for the 0.5-mm vPN. For 2×10^{18} cm^{-3}, we also calculated a 0.25-mm vPN which shows a ∼66 GHz bandwidth and a ∼2 dB ER. Thus, we predict that a ∼60 GHz bandwidth and a ∼3 dB ER can be achieved for the vPN-based NTW-MZMs by using a middle length between 0.25 and 0.5 mm and an immediate density between $1 \sim 2 \times 10^{18}$ cm^{-3}.

The 1-mm vPN at 1×10^{18} cm^{-3} and the 0.5-mm one at 2×10^{18} cm^{-3} show the larger products of bandwidth and ER, indicating that they have better figure of merit than other diode conditions for the tradeoff between bandwidth and modulation depth. Therefore, it is possible to achieve higher bandwidth, larger ER, and even smaller footprint for NTW-MZMs by utilizing the vPN diodes. The loss of phase shifter will not be discussed in this paper, but we have two conclusions for qualitatively comparing the loss: (1) under the same doping density, the vPN has lower loss per unit length than the hPN due to the large area of depletion layer; and (2) the loss per unit length will be doubled if we double the doping density for both hPN and vPN. Thus, we can compare the relative loss figure between the situations in Table II.

D. Bandwidth Comparison Between NTW and TW MZM

The RF loss and transit time determine the theoretical bandwidth limits for TW-MZMs and NTW-MZMs, respectively. The bandwidths of real devices are always less than these limits due to impedance mismatching and RF-optical velocity mismatching. Here we compare these two theoretical bandwidth limits, the RF loss dominated bandwidth of TW-MZM and the transit-time dominated one of NTW-MZM. The major source of RF loss at high frequencies is the dielectric loss resulting from the loaded *pn* diodes [14], [16], which can be calculated by solving the differential equation (Eq. 5 in [14]) of voltage across the diode to the propagation distance using the diode parameters in Section II.B.

The calculated RF losses of TW-MZMs and corresponding EO responses are shown in Figs. 7(a) and 7(b), respectively. In Fig. 7(a), the RF loss of the vPN is about 2.5∼3 times higher than that of the hPN for the frequency up to 60 GHz. The high RF loss of the vPN mainly originates from its large junction capacitance as shown in Fig. 2(b) because the RF loss is proportional to the squared capacitance [32]. Thus, the TW-MZM using the vPN shows much lower 3-dB bandwidths than that using the hPN (less than the half of the latter), as seen in Fig. 7(b). This explains why the vPN-based TW-MZMs usually have lower EO bandwidths than the hPN-based ones in experiment. The

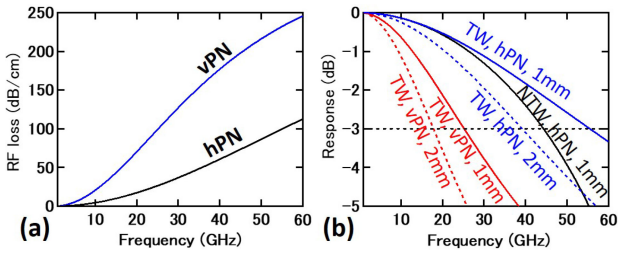

Fig. 7. (a) Calculated frequency dependent RF loss of TW electrodes loaded with the hPN and vPN at a doping density of 1×10^{18} cm^{-3}. (b) Comparison on the EO responses between NTW and TW MZMs.

bandwidth estimated from RF loss for the 2-mm vPN-based TW-MZM is ∼18 GHz that is close to our experimental one (∼17 GHz) of a TW-MZM using a similar vPN diode [31].

We cite the EO response of the 1-mm hPN-based NTW-MZM from Fig. 5 in Fig. 7(b) for comparison. For the hPN, the 1-mm NTW-MZM is observed to have a bandwidth larger than that of the 2-mm TW-MZM, but smaller than that of the 1-mm TW-MZM. But for the vPN, the bandwidth of 1-mm NTW-MZM (∼37 GHz as seen in Fig. 5) can be ∼12 GHz higher than that of the 1-mm TW-MZM and ∼19 GHz higher than that of the 2-mm TW-MZM. In addition, the 1-mm vPN NTW-MZM shows a comparable bandwidth and modulation depth to the 2-mm hPN TW-MZM. Therefore, the vPN can offer better performance if being applied to NTW-MZMs than to TW-MZMs. The vPN suffers severe RF loss that can induce great bandwidth degradation in TW-MZMs, but the RF loss can be avoided in NTW-MZMs.

III. Experiment

A. Device and Measurement

With the segmented rib waveguide structure as shown in Section II.A, two designs of NTW electrodes were fabricated for comparison, as shown in Figs. 8(a) and 8(b). We use Dev A and Dev B to present the NTW-MZM in Fig. 8(a) and 8(b), respectively. Dev A is exactly same as that shown in Figs. 1(a) and 1(b), which adopts the GSGSG configuration and the electrical pads are put on the top of segmented rib waveguides (indicated by slab region in Fig. 1(b)). This design offers the smallest footprint but introduces additional GS capacitance. This GS capacitance mainly comes from the formed vertical capacitor between doping layer accessing the ground and the S metal on top of phase shifter. Dev B adopts GSSG configuration using the comb-like electrode with a comb strip width of 7 μm. The electrical pads are put outside the rib waveguides, while the footprint keeps compact as well (<250 μm in length). Additional GS capacitance in this design is expected to be negligible since the vertical capacitor as formed in Dev A is removed and the capacitor between comb strips has smaller area and larger dielectric thickness than the vertical capacitor in Dev A, which is estimated only about 14 fF. These two devices will be analyzed to clarify the dominant factors in determining high-frequency performance. Both devices were fabricated on the 220-nm silicon-on-insulator wafers with 3-μm-thick box

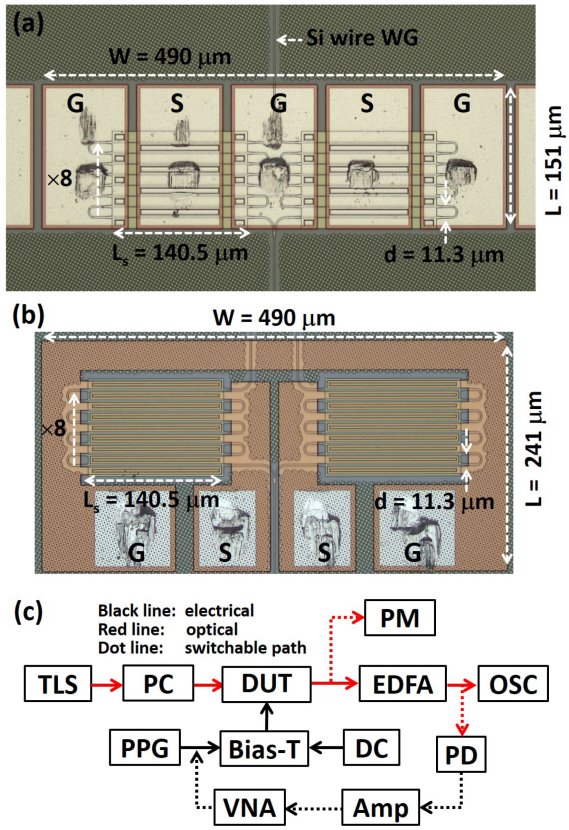

Fig. 8. Optical microscope photograph of the fabricated NTW-MZMs: (a) GSGSG (Dev A) and (b) GSSG (Dev B) configuration. (c) Measurement system. TLS: tunable laser source. PC: polarization controller. DUT: device under test. PM: optical power meter. EDFA: Er-doped fiber amplifier. PPG: pulse pattern generator. OSC: oscilloscope. PD: high speed photodetector. DC: dc source. Amp: electrical amplifier. VNA: vector network analyzer.

layers using the standard AIST-SCR 12-inch silicon photonics line [33]. The widths of connecting wire waveguides and rib waveguides are 430 nm and 600 nm, respectively. The slab and clad thicknesses are ∼110 nm and ∼1.5 μm, respectively. AlCu is used for the electrode that has a thickness of ∼1.5 μm. For optical coupling, inversely tapered structures were fabricated at both facets of chips. So far, we only fabricated the NTW-MZM based on the conventional horizontal *pn* junction that is same as our previous work [34]. The average doping density is about $5\sim8 \times 10^{17}$ cm^{-3}.

The measurement system is shown in Fig. 8(c). The details of measurement can be referred to in [24], [34]. The laser light (∼1.55 μm) emitted from a TLS was tuned to TE polarization and then coupled into the device through a tapered fiber. The output light was taken by another tapered fiber and then input to an optical power meter for direct-current (dc) measurement or EDFA for high frequency measurement. After EDFA, the light was selectively connected to a high-speed oscilloscope with a 30-GHz optical plug-in module for eye diagram measurement or a high-speed PD for EO response measurement. A PRBS NRZ signal from PPG (Anritsu MP1800A) and sinusoidal signals from VNA were applied to the device after combining with a dc bias via a bias-tee for eye diagram and bandwidth measurements, respectively. The converted electrical signal from

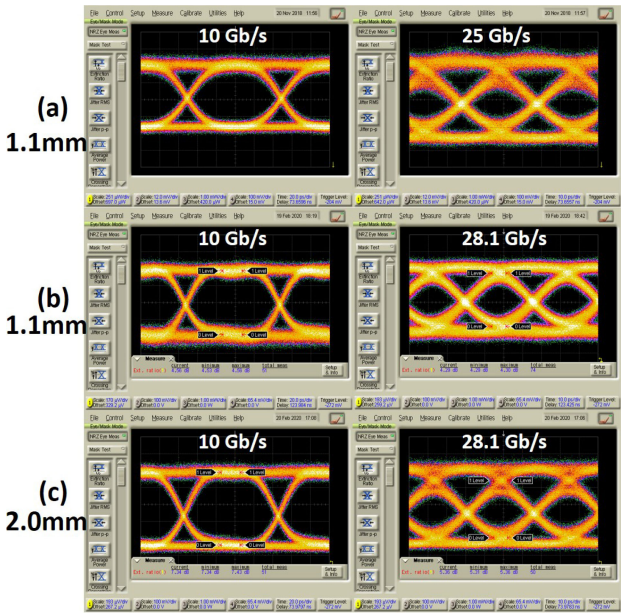

Fig. 9. Eye diagrams: (a) GSGSG modulator (Dev A) in Fig. 8(a). (b) and (c) GSSG modulator (Dev B) in Fig. 8(b) with ∼1.1 and ∼2.0 mm total *pn* junction lengths, respectively.

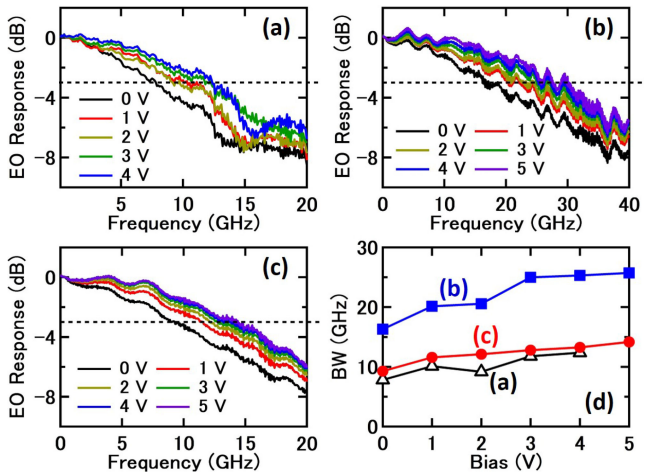

Fig. 10. Measured EO responses at different biases of (a) GSGSG modulator (Dev A) in Fig. 8(a), (b) and (c) GSSG modulators (Dev B) in Fig. 8(b) with ∼1.1 and ∼2.0 mm total *pn* junction lengths, corresponding to Figs. 9(a)−9(c) respectively. Dotted lines indicate −3 dB. (d) Bias dependent 3-dB bandwidth. Curves (a), (b), (c) denote corresponding figures.

PD was returned to VNA via a high frequency electrical amplifier. High-frequency probes were used for signal input and output after calibrated by a standard open-short-through-load substrate. An external 50 Ω terminator was loaded also through a high-frequency probe. We performed single-arm driving on the left arm instead of push-pull driving and all measurements were taken around the quadrature point of MZM that was controlled using the right arm. The EO responses were calibrated using the properties of probe and high-speed PD. As for the dc performance of the phase shifter under the current diode condition, we evaluated $V_\pi L$ around 2.1−2.3 V·cm and the loss around ∼20−23 dB/cm for 0−3 V biases. All biases used below denote reverse biases.

B. NRZ Eye Diagram

Eye diagrams were measured for Dev A (Fig. 8(a)) and Dev B (Fig. 8(b)), both of which have a total *pn* junction length of about 1.1 mm ($L_s \times 8$). For Dev B, we also measured a device with 14 rib segments that has a total *pn* junction length of about 2.0 mm ($L_s \times 14$) for comparison. The peak-to-peak RF voltage and the dc bias were set to 3 V and 4 V, respectively, for all measurements. Fig. 9(a) shows the eye diagrams of Dev A that were measured at 10 and 25 Gb/s with 2^{15}-1 PRBS pattern. As can be seen, the eyes are clearly opened at both bit rates, but obvious degradation is observed at 25 Gb/s. The extinction ratios (ERs) are about 3.7∼4 dB.

Fig. 9(b) shows the eye diagrams of Dev B that were measured at 10 and 28.1 Gb/s with 2^{31}-1 PRBS pattern. Even though it has the same total *pn* junction length as Dev A, its eyes show much better opening with enhanced ER (4.3∼4.6 dB) and faster response. Dev B shows better eye performance than Dev A. The 20−80% leading/trailing time at the edges of 10 Gb/s eye is almost equivalent to that of our PPG apparatus. Fig. 9(c) shows the eye diagram of Dev B with a 2-mm phase shifter, which was measured under the same conditions as Fig. 9(b). It offers a high ER (∼7.3 dB) at 10 Gb/s and the eye also keeps open for up to 28.1 Gb/s, but degradation can be seen at 28.1 Gb/s with a decreased ER (∼5.4 dB).

C. EO Bandwidth

The measured EO responses are shown in Figs. 10(a)−10(c) that correspond to the measured eye diagrams in Figs. 9(a)−9(c), respectively. The 3-dB bandwidths are extracted from these EO response curves and plotted in relation of bias in Fig. 10(d). Dev A has a bandwidth of ∼13 GHz at 3−4 V biases, as seen in Fig. 10(a) [24], explaining the its eye degradation at 25 Gb/s. However, with the same total *pn* junction length (∼1.1 mm) as Dev A, Dev B in Fig. 8(b) shows improved bandwidth, ∼26 GHz at 3 − 4 V biases, as seen in Fig. 10(b), which contributes to its much better eye performance in Fig. 9(b). This bandwidth improvement is believed partially resulting from the reduction in GS capacitance and will be further explained in next Section III.D. If increasing the total *pn* junction length to ∼2.0 mm, the bandwidth decreases to ∼14 GHz at 3−4 V biases, as seen in Fig. 10(c). As shown in Fig. 10(d), it is well known that increasing the bias can increase the bandwidth due to the junction capacitance reduction (see Fig. 2(b)).

In experiment, there are two factors left in above analysis that influence the EO bandwidth. (1) The first is the connecting waveguides between the segments of rib waveguides. Because the connecting waveguide length also contributes to the transit time, the bandwidth will be decreased. The connecting waveguide lengths are ∼350 μm and ∼650 μm for the 1.1 mm and 2.0 mm devices in Fig. 9, respectively. The estimated bandwidths after counting this additional length (∼32 GHz for 1.1 mm and ∼18 GHz for

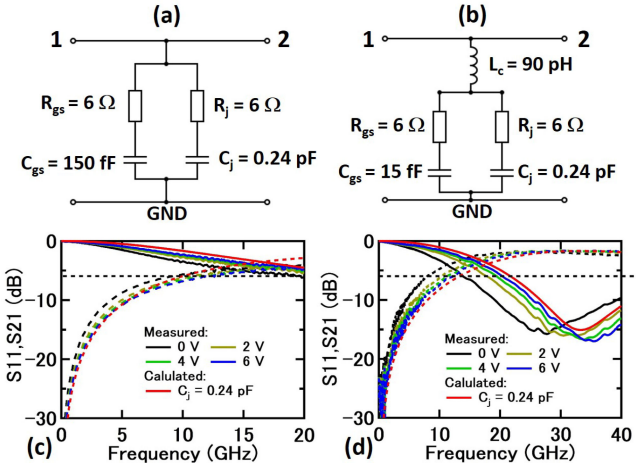

Fig. 11. Shunt-through circuit model for (a) Dev A and (b) Dev B. Measured and calculated S parameters for (c) Dev A and (d) Dev B. Dashed lines (S11) and solid lines (S21) share same color labels. Dotted lines indicate −6 dB.

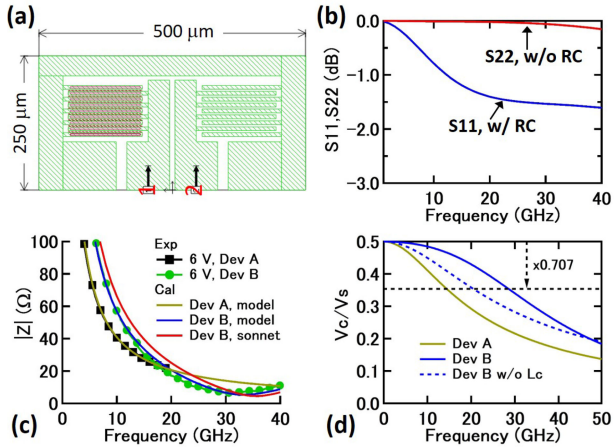

Fig. 12. (a) Device model in SONNET simulation. The left arm is loaded with RC and the right arm is only of metal. (b) S11, S22 simulated by SONNET. Ports 1 and 2 are indicated in (a). (c) Frequency dependent impedance. (d) Ratio of the capacitor partial voltage to the RF source voltage V_c/V_s.

2.0 mm) are still larger than the experimental bandwidths by 5∼6 GHz. (2) The second is the impedance matching that is of vital importance for such small lumped-element NTW-MZMs. The observed bandwidth enhancement (Dev A → Dev B) suggests the influence of impedance matching because the capacitance reduction can increase the input impedance that influences the effective voltage on junction. The impedance matching problem is studied in next section, which verifies that the experimental bandwidths are dominated by impedance mismatching and thus explains the gap between experiment and calculation.

D. Impedance Matching Problem

To examine the impedance, we measured the S parameters of Dev A and B and compare with circuit models. Two shunt-through circuit models shown in Figs. 11(a) and 11(b) are proposed to describe Dev A and B, respectively. In these models, R_j and $R_{\rm gs}$ are the series resistances of the junction capacitance C_j and the GS capacitance $C_{\rm gs}$, respectively. For Dev B, an inductance L_c is considered due to the comb lines of electrode while it can be negligible in Dev A. The measured S11 and S21 are shown in Figs. 11(c) and 11(d) for Dev A and B, respectively. The electrical frequency response only depends on impedance matching condition. For Dev A, C_{gs} is estimated about 150 fF while for Dev B, it is reduced to about 15 fF. Using the same *pn* junction parameters, we calculated the S parameters based on circuit models shown in Figs. 11(a) and 11(b). The calculated S11 and S21 reasonably reproduce the experimental ones at the biases of $4-6$ V for both Dev A and B. For Dev B, the calculation using $L_{\rm c}=90$ pH for the comb lines reproduces the dip around 30 GHz in S21, indicating that this dip originates from the series LC resonance that centers at ∼33.2 GHz according to the model in Fig. 11(b). In contrast, such a dip has not been observed for Dev A because the inductance effect in the electrode of Dev A is negligible. Even though this inductance induces a dip in electrical S21 of Dev B, this LC resonance can enhance the EO bandwidth because it will increase the partial voltage across junction capacitor, which introduces a peaking effect in optical frequency response. The contribution of this inductance to enhance the EO bandwidth will be clearly seen in the following discussion.

Furthermore, we simulated Dev B with the comb-like electrode using the SONNET software [35] to examine the appropriateness to treat it as a lumped element. Fig. 12(a) shows the model built in SONNET, where we leave the right arm as metal only but load ideal R and C components with same parameters as above *pn* junction (Fig. 11(b)) into the left arm. The simulated one-port S parameters are shown in Fig. 12(b) where we did not observe any ripples in both S11 (with RC loaded) and S22 (metal only) that might occur due to the comb-like strips. Thus, Dev B is small enough to be treated as a lumped element as seen from the RF signal side.

The characteristic impedance extracted from the measured S parameters for the bias of 6 V and those from circuit model calculation and SONNET simulation are shown in Fig. 12(c). The impedance calculated by circuit model shows good consistence with the experimental data for both Dev A and B. Furthermore, for Dev B, the circuit model in Fig. 11(b) is well reproduced by SONNET simulation. At the low frequency side (approaching to zero frequency), the device is close to open circuit due to the existence of capacitors, while with increasing the frequency, the impedance quickly decreases. It is this impedance decrease that causes the EO bandwidth degradation because it results in the reduction of effective RF voltages across the junction. Because the model explains the experimental impedances very well, we can estimate the partial voltage V_c across the junction capacitor C_j from the model, which is the effective voltage that contributes to the phase change. The ratio V_c/V_s (V_s is the RF source voltage as defined in Section II.B) shown in Fig. 12(d) describes the voltage transfer efficiency and its frequency dependence can directly reflect the EO response. In our measurement, both ports of Figs. 11(a) and 11(b) are terminated with 50 Ω, thus V_c/V_s equals 0.5 for both devices at the low frequency side because

the devices are nearly open. V_c/V_s decreases with increasing the frequency due to the impedance decrease for both devices, but Dev B has larger V_c/V_s than Dev A in a wide frequency region so that the EO bandwidth of Dev B is larger than that of Dev A, as shown in Fig. 10. For NTW-MZMs, the phase change is proportional to the integration of voltage as expressed by Eq. (2), so the bandwidth at which V_c/V_s decreases to the 0.707 times zero-frequency value indicates the 3-dB EO bandwidth. Such bandwidths in Fig. 12(d) are ~14 GHz for Dev A and ~28 GHz for Dev B, both of which correctly reflect the experimental EO bandwidths in Figs. 10(a) and 10(b), respectively, while these bandwidths do not match well with those estimated from transit time with connecting waveguide taken into considerations.

To explain the bandwidth enhancement from Dev A to Dev B, we also calculate V_c/V_s for Dev B without considering the inductance L_c, which is shown in Fig. 12(d) for comparison. It can be seen that the increase of impedance in Dev B due to the reduction in GS capacitance contributes to ~6 GHz bandwidth enhancement and the existence of L_c can further increase V_c within a wide frequency region due to LC resonance, which contributes to ~8 GHz bandwidth enhancement. The overall frequency response sums up a gradually decreased component and a peaking component that can be more obvious if changing the impedance matching conditions as seen in next section. Under the same termination, when increasing the *pn* junction length to 2.0 mm, the impedance will decrease and the LC resonance frequency also decreases, thus induces a decrease in EO bandwidth even though the RC product remains unchanged. Therefore, we conclude that (1) Dev B is better than Dev A due to its larger impedance and the existence of LC resonance that can enhance EO bandwidth; (2) for a fixed electrode design of NTW-MZMs, the impedance mismatching dominates the experimental bandwidth in our measurement.

E. Driving Configuration for Impedance Matching

To improve the bandwidth for NTW-MZMs, it is necessary to improve impedance matching condition that can be realized by modifying driving configuration even without changing the device itself. As discussed above, our experimental results and calculation are done with a 50-Ω terminated 2-ports configuration. Obviously, this is not optimum matching condition for high frequencies because the impedances at high frequencies are much lower than 50 Ω. We can only perform 50-Ω matching in our cable-based measurement setup in Fig. 8(c), however, it is possible to design low-impedance matching (e.g., 25 Ω) in integrated modulator drivers. Furthermore, in conventional TW-MZMs, single push-pull (SPP) driving (two *pn* diodes are connected in series) is widely used to improve the bandwidth [18], [36]. SPP driving scheme can also be applied to the NTW-MZM for better impedance matching because the effective capacitance is reduced. Thus, we examine this driving scheme under both 50 Ω and 25 Ω matching below. We define our current driving configuration shown in Fig. 11(b) with a terminated port 2 as the 2-port configuration, while that leaving the port 2 open as the 1-port configuration. The port 1 is connected to the driver, so it has a terminated resistor at default.

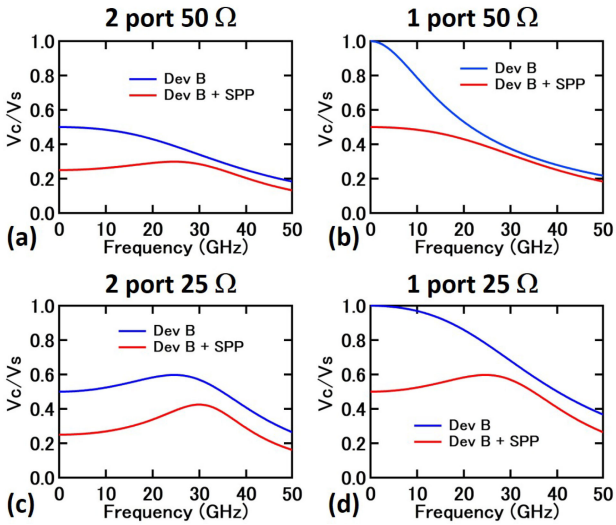

Fig. 13. Ratio of the junction capacitor voltage to the RF source voltage V_c/V_s at various matching conditions for Dev B: (a) 2 ports with 50 Ω; (b) 1 port with 50 Ω; (c) 2 ports with 25 Ω; and (d) 1 port with 25 Ω. SPP: single push-pull.

1) 50-Ω matching. Even though Dev B shows better EO bandwidth than Dev A, SPP can be done for both devices to achieve larger bandwidths. Here, taking Dev B as an example, we compare V_c/V_s under SPP driving with that of Dev B under current single arm driving because the frequency dependent V_c/V_s directly reflects EO bandwidth as mentioned above. Figs. 13(a) and 13(b) show the calculated V_c/V_s at 50-Ω matching for 2-port and 1-port configurations, respectively. For single arm driving (blue lines), the 1-port configuration shows lower bandwidth (~13 GHz) than the 2-port one (~28 GHz) because its V_c at zero frequency is doubled compared to the 2-port one due to the lack of voltage dividing resistor. If adopting SPP driving (red lines), the bandwidth can be increased to ~43 GHz and ~29 GHz for the 2-port and 1-port configurations, respectively. This bandwidth increase mainly comes from the reduction of V_c at the low frequency side because the RF voltage is divided by two diodes. At zero frequency (complete open circuit), V_c of SPP driving is reduced to a half that of single arm driving, but at higher frequencies this reduction ratio is relatively increased because the overall RF voltage across two diodes is increased due to the impedance increase from series connected capacitance and resistance.

2) 25-Ω matching. If the device is matched to 25 Ω, the bandwidth will be improved greatly compared to 50-Ω matching. Figs. 13(c) and 13(d) show the calculated V_c/V_s at 25-Ω matching for 2-port and 1-port configurations, respectively. The bandwidth can be increased from current ~28 GHz at 50-Ω matching to ~43 GHz at 25-Ω matching at the 2-port configuration and from current ~13 GHz at 50-Ω matching to ~29 GHz at 25-Ω matching for the 1-port configuration. This bandwidth improvement does not sacrifice the modulation efficiency because the ratio V_c/V_s is enhanced over a wide frequency range compared to 50-Ω matching, which can be seen by comparing blues lines in Figs. 13(c) and 13(d) to those in Figs. 13(a) and 13(b), respectively. Thus, low-impedance matching is a simple

way to improve both bandwidth and efficiency for NTW-MZMs. Similarly as in 50-Ω matching, adopting SPP driving can further improve the bandwidth to ∼48 GHz and ∼43 GHz for 2-port and 1-port configurations, respectively. Furthermore, the 1-port configuration offers larger V_c/V_s than the 2-port one for both 25-Ω and 50-Ω matching, so the 1-port configuration can offer better modulation efficiency. The contributions from LC resonance have been already included in above results in this section and its peaking effect varies with impedance matching conditions, as seen in Fig. 13. The LC resonance induced bandwidth enhancement is more obvious for low impedance matching, SPP driving, and 2-port configuration.

Therefore, according to all above discussions, there are three remaining works in future study for improving the performance of NTW-MZMs: (1) SPP driving with or without low impedance matching; (2) Designing NTW-MZMs with shorter or without connecting waveguides; and (3) Applying vertical *pn* junctions. Through these studies, we could achieve better tradeoff between high-frequency performance and compact footprint for NTW-MZMs.

IV. Conclusion

We experimentally demonstrated carrier-depletion NTW-MZMs on silicon photonic platform. They adopt densely meandered phase shifters and thus offer an ultra-compact lumped-element MZ modulator for using carrier depletion. Up to 28.1 Gb/s NRZ eye diagrams and ∼26 GHz EO bandwidth were experimentally achieved, showing improved high frequency performance than previous works. The proposed lumped circuit model well explained the experimental S-parameters and frequency dependent impedance, indicating that the impedance mismatching is the dominant factor in determining experimental bandwidth and the LC resonance can contribute to bandwidth enhancement for NTW-MZMs using a comb-like electrode with suitable inductance. Driving schemes that could enable better impedance matching was proposed to enhance bandwidth. This NTW-MZM could enhance the integration density of modulators for wavelength-division multiplexing transceivers and offer better tradeoff between compact footprint, modulation depth, and high speed for utilizing carrier depletion.

Acknowledgment

The authors thank T. Narushima, N. Yokoyama, M. Seki, M. Ohtsuka, K. Matsumaro, E. Ishitsuka, and all other staffs from AIST SCR station for their support in device fabrication.

References

[1] C. R. Doerr, "Silicon photonic integration in telecommunications," *Front. Phys.*, vol. 3, Aug. 2015, Art. no. 37.

[2] J. Witzens, "High-speed silicon photonics modulators," *Proc. IEEE*, vol. 106, no. 12, pp. 2158–2182, Dec. 2018.

[3] A. H. Atabaki *et al.*, "Integrating photonics with silicon nanoelectronics for the next generation of systems on a chip," *Nature*, vol. 556, pp. 349–354, Jun. 2018.

[4] S. Fathololoumi *et al.*, "1.6Tbps silicon photonics integrated circuit for Co-packaged optical-IO switch applications," in *Proc. OFC*, San Diego, CA USA, 2020, Paper T3H.1.

[5] P. Dong *et al.*, "112-Gb/s monolithic PDM-QPSK modulator in silicon," *Opt. Express*, vol. 20, no. 26, pp. B624–B629, Dec. 2012.

[6] W. Bogaerts *et al.*, "Silicon microring resonators," *Laser Photon. Rev.*, vol. 6, no. 1, pp. 47–73, Jan. 2012.

[7] Y. Hinakura *et al.*, "Electro-optic phase matching in a Si photonic crystal slow light modulator using meander-line electrodes," *Opt. Express*, vol. 26, no. 9, pp. 11538–11545, Apr. 2018.

[8] Y. Hinakura *et al.*, "64 Gbps Si photonic crystal slow light modulator by electro-optic phase matching," *Opt. Express*, vol. 27, no. 10, pp. 14321–14327, May 2019.

[9] Y. Sobu *et al.*, "High-speed-operation of compact all-silicon segmented mach-zehnder modulator integrated with passive RC equalizer for optical DAC transmitter," in *Proc. OFC*, San Diego, CA, USA, 2020, Paper M2B.8.

[10] S. Tanaka *et al.*, "Ultralow-power (1.59 mW/Gbps), 56-Gbps PAM4 operation of Si photonic transmitter integrating segmented PIN Mach-Zehnder modulator and 28-nm CMOS Driver," *J. Lightw. Technol.*, vol. 36, no. 5, pp. 1275–1280, Mar. 2018.

[11] C. Doerr *et al.*, "Single-chip silicon photonics 100-Gb/s coherent transceiver," in *Proc. OFC*, San Francisco, CA, USA, 2014, Paper Th5C.1.

[12] B. G. Lee *et al.*, "Driver-integrated 56-Gb/s segmented electrode silicon mach zehnder modulator using optical-domain equalization," in *Proc. OFC*, 2017, Paper Th1B.1.

[13] D. Patel *et al.*, "Design, analysis, and transmission system performance of a 41 GHz silicon photonic modulator," *Opt. Express*, vol. 23, no. 11, pp. 14263–14287, May 2015.

[14] S. S. Azadeh *et al.*, "Low V_π Silicon photonics modulators with highly linear epitaxially grown phase shifters," *Opt. Express*, vol. 23, no. 18, pp. 23526–23550, Aug. 2015.

[15] R. Ding *et al.*, "High-speed silicon modulator with slow-wave electrodes and fully independent differential drive," *J. Lightw. Technol.*, vol. 32, no. 12, pp. 2240–2247, Jun. 2014.

[16] H. Sepehrian *et al.*, "Silicon photonic IQ modulators for 400 Gb/s and beyond," *J. Lightw. Tech.*, vol. 37, no. 13, pp. 3078–3086, Jul. 2019.

[17] W. Shi *et al.*, "Silicon photonic modulators for PAM transmissions," *J. Opt.*, vol. 20, Jul. 2018, Art. no. 083002.

[18] J. Lin *et al.*, "Single-carrier 72 GBaud 32QAM and 84 GBaud 16QAM transmission using a SiP IQ modulator with joint digital-optical pre-compensation," *Opt. Express*, vol. 27, no. 4, pp. 5610–5619, Feb. 2019.

[19] S. Zhalehpour *et al.*, "All-silicon IQ modulator for 100 GBaud 32QAM transmissions," in *Proc. OFC*, 2019, Paper Th4A.5.

[20] M. Jacques *et al.*, "Net 212.5 Gbit/s transmission in O-band with a SiP MZM, one driver and linear equalization," in *Proc. OFC*, 2020, Paper Th4A.3.

[21] C. Wang *et al.*, "Integrated lithium niobate electro-optic modulators operating at CMOS-compatible voltages," *Nature*, vol. 562, pp. 101–104, Sep. 2018.

[22] M. He *et al.*, "High-performance hybrid silicon and lithium niobate Mach-Zehnder modulators for 100 Gbit s^{-1} and beyond," *Nat. Photon.*, vol. 13, pp. 359–364, Mar. 2019.

[23] Y. Ogiso *et al.*, "Ultra-high bandwidth InP IQ modulator for beyond 100-GBd transmission," in *Proc. OFC*, 2019, Paper M2F.2.

[24] G. W. Cong *et al.*, "Ultra-compact non-travelling-wave silicon Mach-Zehnder modulator," in *Proc. ECOC*, Dublin, Ireland, 2019, Paper Tu3.A.4.

[25] S. S. Azadeh *et al.*, "Power-efficient lumped-element meandered silicon Mach-Zehnder modulators," in *Proc. SPIE 11285, Silicon Photon. XV*, Feb, 26. 2020.

[26] D. M. Gill *et al.*, "Distributed electrode Mach-Zehnder modulator with double-pass phase shifters and integrated inductors," *Opt. Express*, vol. 23, no. 13, pp. 16857–16865, Jun. 2015.

[27] M. R. Watts *et al.*, "Low-voltage, compact, depletion-mode, silicon mach-zehnder modulator," *IEEE J. Sel. Top. Quantum Electron.*, vol. 16, no. 1, pp. 159–164, Jan. 2010.

[28] Lumerical CHARGE and MODE simulators at. [Online]. Available: www.lumerical.com

[29] Y. Terada *et al.*, "Si photonic crystal slow-light modulators with periodic p-n junctions," *J. Lightw. Technol.*, vol. 35, no. 9, pp. 1684–1692, May 2017.

[30] Z. Yong *et al.*, "U-shaped PN junctions for efficient silicon Mach-Zehnder and microring modulators in the O-band," *Opt. Express*, vol. 25, no. 7, pp. 8425–8439, Apr. 2017.

[31] Y. Maegami *et al.*, "High-efficiency strip-loaded waveguide based silicon Mach-Zehnder modulator with vertical p-n junction phase shifter," *Opt. Express*, vol. 25, no. 25, pp. 31407–31416, Dec. 2017.

[32] F. Merget *et al.*, "Silicon photonics plasma-modulators with advanced transmission line design," *Opt. Express*, vol. 15, no. 17, pp. 19593–19607, Aug. 2013.
[33] K. Yamada *et al.*, "A 300-mm-wafer silicon photonics technology for ultra-low-energy optical network systems," in *Proc. Asia Commun. Photon. Conf.*, Guangzhou, Guangdong, China, 2017, Paper S4H.3.
[34] G.W. Cong *et al.*, "Silicon traveling-wave Mach-Zehnder modulator under distributed bias driving," *Opt. Lett.*, vol. 43, no. 3, pp. 403–406, Feb. 2018.
[35] SONNET Inc., [Online]. Available: www.sonnetsoftware.com
[36] P. Dong *et al.*, "High-speed low-voltage single-drive push-pull silicon Mach-Zehnder modulators," *Opt. Express*, vol. 20, no. 6, pp. 6163–6169, Mar. 2012.

Guangwei Cong (Member, IEEE) received the Ph.D. degree from the Institute of Semiconductors, Chinese Academy of Sciences, Beijing, China, in 2006. In 2006, he joined the National Institute of Advanced Industrial Science and Technology (AIST), Tsukuba, Japan, as a Postdoc. Since 2010, he has been a Researcher with AIST and engaged in developing monolithic integration of CMOS with silicon photonics devices, modulators, and other novel devices. He is currently a Senior Researcher with AIST, where he is involved in developing silicon photonics technology for advanced information and computing systems. From 2007 to 2009, he was a JSPS Postdoc with the Japan Society for the Promotion of Science and did research on ultrafast all-optical switches. He is a member of OSA.

Yuriko Maegami received the M.E. and Ph.D. degrees from the Department of Mechanical Systems Engineering, Tohoku University, Sendai, Japan, in 2009 and 2013, respectively. In 2013, she joined the National Institute of Advanced Industrial Science and Technology (AIST), Tsukuba, Japan, where she has been engaged in studying CMOS-compatible silicon photonics devices. She is a member of the IEEE Photonics Society, the Institute of Electronics, Information and Communication Engineers, and the Japan Society of Applied Physics.

Morifumi Ohno received the M.S. degree in electrical engineering from the Tokyo University of Agriculture and Technology, Tokyo, Japan, in 1983, and the Ph.D. degree in electronic materials science from the Graduate School of Electronic Science and Technology, Shizuoka University, Shizuoka, Japan, in 1986. He had joined Oki Electric Industry Company, Ltd. (present, OKI Semiconductor Company, Ltd.), where he engaged in the R&D of advanced NVRAM (FeRAM) and FD-SOI devices. In 2009, he joined, as an Invited Researcher, with the National Institute of Advanced Industrial Science and Technology, Tsukuba, Japan, where he is currently involved in the design, simulation, and characterization of nano-electronic devices and silicon photonics devices, including modulators and other novel devices.

Koji Yamada (Senior Member, IEEE) received the B.E., M.E., and Ph.D. degrees in nuclear engineering from Kyushu University, Fukuoka, Japan, in 1986, 1988, and 2003, respectively. He is currently leading the Silicon Photonics Group, National Institute of Advanced Industrial Science and Technology (AIST), Tokyo, Japan. From 1988 to 2015, in NTT Laboratories, he was engaged in studies on accelerator physics/engineering for synchrotron light sources and on silicon-based photonic platforms. Since 2015, he has been with AIST and has been studying silicon-based photonic platforms. He is a member of the Institute of Electronics, Information and Communication Engineers and the Japan Society of Applied Physics.